Two spinning ways for precession dynamo

L. Cappanera, J.-L. Guermond, J. Léorat, and C. Nore

Phys. Rev. E **93**, 043113 — Published 14 April 2016

DOI: 10.1103/PhysRevE.93.043113

TWO SPINNING WAYS FOR PRECESSION DYNAMO

L. CAPPANERA[1], J.-L. GUERMOND[2], J. LÉORAT[3] AND C. NORE[1]

Abstract. It is numerically demonstrated by means of a magnetohydrodynamic code that precession can trigger dynamo action in a cylindrical container. Fixing the angle between the spin and the precession axis to be $\frac{1}{2}\pi$, two limit configurations of the spinning axis are explored: either the symmetry axis of the cylinder is parallel to the spin axis (this configuration is henceforth referred to as the axial spin case), or it is perpendicular to the spin axis (this configuration is referred to as the equatorial spin case). In both cases, the centro-symmetry of the flow breaks when the kinetic Reynolds number increases. Equatorial spinning is found to be more efficient in breaking the centro-symmetry of the flow. In both cases, the average flow in the reference frame of the mantle converges to a counter-rotation with respect to the spin axis as the Reynolds number grows. We find a scaling law for the average kinetic energy in term of the Reynolds number in the axial spin case. In the equatorial spin case, the unsteady asymmetric flow is shown to be capable of sustaining dynamo action in the linear and nonlinear regimes. The magnetic field is mainly dipolar in the equatorial spin case while it is is mainly quadrupolar in the axial spin case.

1. Introduction

The idea that precession can be an efficient mechanism to generate the Earth's magnetic field through dynamo action has long been debated (see for example [1]). Observations of some planetary dynamos could contribute to resolve this issue but definite evidence is still lacking [2]. Despite the lack of astrophysical evidence, precession has nevertheless recently attracted the attention of the experimental dynamo community since this mechanism has the potential to generate large scale fluid motions without requiring any pump or impellers. For example, an ambitious project at the DREsden Sodium facility for DYNamo and thermohydraulic studies (DRESDYN) [3] consists of building a precession-driven MHD (MagnetoHydroDynamics) experiment running at large magnetic Reynolds numbers. The device will be a large cylinder of diameter and height equal to 2 metres. It will be filled with liquid sodium and will undergo rotation about its symmetry axis and precession about another axis (which can be the equator). The planned maximum rotation and precession frequencies are 10 Hz and 1 Hz, respectively, leading to a magnetic Reynolds number of a few hundreds. Even though numerical simulations of the Dresden experiment with very large kinetic Reynolds numbers (at least 10^6) are out of reach with present day computers, we think that numerical simulations are useful complements and can shed some light on specific aspects of this experiment.

Because of the large computing resources required, it is only recently that precession driven dynamos have been numerically explored: see [4] for dynamos in spheres and [5] for dynamos in spheroids. Since neither spheres nor spheroids are convenient for large-scale experiments, it is instructive to investigate whether similar results

can be obtained in cylindrical containers. Many experiments have been conducted in cylinders with varying aspect ratios, various angles between the precession and the spin axis (always assumed to be the symmetry axis) and varying ratios of precession to spin frequencies (see e.g. [6, 7, 8, 9]). An increasing number of numerical studies have been performed as well; see for instance [10, 11, 12, 13, 14, 15]. With the exception of [10], all the works referred to above have been mainly devoted to hydrodynamic studies. In [10] we have studied the dynamo capabilities of a cylinder spinning around its symmetry axis and precessing at a strong rate around an axis perpendicular to the symmetry axis. (This configuration is henceforth called *axial spin case* in the rest of the paper.)

The main motivation of the present paper is to present new hydrodynamic and magnetohydrodynamic results in a precessing cylinder in order to inform precession-driven dynamo experiments. The first objective is to investigate the influences (both hydrodynamics and magnetohydrodynamics) of the angles between the symmetry axis, the spin axis and the precession axis. The second objective is to investigate the magnetohydrodynamic effects of the electric conductivity and magnetic permeability of the side walls and lid walls of the container. Being limited in computer resource, we only test two extreme configurations, namely the *axial spin case* as in [10], and the *equatorial spin case* where the symmetry axis and the precession axis are both perpendicular to the spinning axis. We investigate which of these two configurations is the most efficient in breaking the centro-symmetry and which one gives the lowest dynamo threshold.

The paper is organized as follows. Section §2 describes the numerical setting and the two configurations that are used in the paper to apply the rotation and the precession, namely the axial and the equatorial spin forcings. SFEMaNS, the magnetohydrodynamic code that we use in all our computations, is briefly described in appendix §A.1. Section §3 presents hydrodynamic studies in relation with the precession-driven experiment at the DRESDYN facility. A large range of kinetic Reynolds numbers is explored for the axial spin case. Simulations at Reynolds numbers as high as 15000 are done by using the entropy viscosity stabilization method summarized in appendix §A.2. The two spinning strategies for precession forcing are investigated and compared. Equatorial spinning is observed to be more efficient to break the centro-symmetry of the flow than axial spinning. Section §4 contains new results of dynamo action in the axial spin case with varying properties of the vessel walls. It is shown that using lateral walls made of copper helps the dynamo effect. It is also numerically demonstrated in this section that precession can generate dynamo action in the equatorial spin case. But, although centro-symmetry is more easily broken by equatorial spinning than by axial spinning, it is observed that the critical magnetic Reynolds for the axial spin configuration is lower than for the equatorial spin case. Section §5 contains a discussion of our results and concluding remarks.

2. Numerical setting

Let us consider a cylindrical vessel $\mathcal{C}$ of radius R, height L and center of mass O. The vessel contains a conducting fluid and is embedded in a non-conducting media (air, vacuum, etc.). The container rotates about the so-called spin axis passing through O and aligned with the unit vector $\mathbf{e}_s$; the spinning angular velocity is constant and equal to $\Omega_s \mathbf{e}_s$. The cylinder is also assumed to precess about a

second axis passing through O and aligned with the unit vector $\mathbf{e}_p$ forming an angle α with $\mathbf{e}_s$ ($0 < \alpha < \pi$) (see figure 1). The precession vector $\mathbf{e}_p$ is fixed in a Galilean reference frame, i.e., the laboratory frame. The constant precession angular velocity is $\Omega_p \mathbf{e}_p$. We use the cylindrical coordinate system centered at O for the computations. The Oz axis is the line passing through O and parallel to the axis of the cylinder; the Oz axis is oriented by choosing a unit vector $\mathbf{e}_z$. The origin $\theta = 0$ of the angular coordinate ($0 \leq \theta < 2\pi$) is the half plane passing through O and spanned by $\mathbf{e}_z$ and $\mathbf{e}_p$ (axial spin case, see below) or spanned by $\mathbf{e}_z$ and $\mathbf{e}_s$ (equatorial spin case). The third coordinate, denoted r, is the distance to the Oz axis.

Let R and $U = R\Omega_s$ be the reference length and velocity scales, respectively. The fluid density, ρ, is assumed to be constant and the reference pressure scale is $P := \rho U^2$. The magnetic permeability and the electric conductivity of the conducting fluid are constant, μ_0 (equal to the vacuum permeability) and σ_0 respectively. These quantities are used as reference magnetic permeability and electric conductivity, respectively. The reference scale for the magnetic induction is chosen so that the reference Alfvén speed is 1, i.e., $B := U\sqrt{\mu_0 \rho}$.

Six parameters govern the flow: the aspect ratio of the container L/R, the precession angle α (angle between the spin axis $\mathbf{e}_s$ and the precession axis $\mathbf{e}_p$), the spin angle (angle between the symmetry axis $\mathbf{e}_z$ and the spin axis $\mathbf{e}_s$), the precession rate $\varepsilon = \Omega_p/\Omega_s$ (ratio of the precession and spin angular velocity, also called the Poincaré number), the kinetic Reynolds number $R_\mathrm{e} = R^2\Omega_s/\nu$ (where ν is the kinematic viscosity) and the magnetic Reynolds number $R_\mathrm{m} = \mu_0\sigma_0 R^2 \Omega_s$. Note that R_e is in fact the inverse of the Ekman number.

We start by fixing the ratio of the height of the cylinder to its radius, L/R, to be equal to 2, since this is the non-resonant aspect ratio that has been chosen for the DRESDYN experiment. In passing, we refer to [14, 15] for interesting hydrodynamic studies on resonant aspect ratios. Choosing the precession axis orthogonal to the spin axis (i.e., $\alpha = \pi/2$) and the precession rate $\varepsilon = 0.15$, we are left with two limit configurations: one called *axial spin* for which the spin angle is 0 and the symmetry axis of the cylinder remains fixed in the precessing frame and another one called *equatorial spin* for which the spin angle is $\pi/2$ and the symmetry axis rotates in the precessing frame (see figure 1). In the axial spin case, the wall speed is tangent to the wall and only the viscous stress at the wall drives the flow, whereas, in the equatorial spin case, the flow is put into motion by the pressure at the wall and is therefore inertially driven.

The non-dimensional set of equations can be written in two frames of reference. For the *axial spin* case, the computations can be performed in the *precessing* frame since the geometry of the container is fixed in this frame; the equations are then written as follows:

$$\partial_t \mathbf{u} + (\mathbf{u}\cdot\nabla)\mathbf{u} + 2\varepsilon \mathbf{e}_p \times \mathbf{u} + \boldsymbol{\nabla} p = \frac{1}{R_\mathrm{e}} \Delta \mathbf{u} + \left[\boldsymbol{\nabla} \times \left(\frac{\mathbf{B}}{\mu_r}\right)\right] \times \mathbf{B}, \tag{2.1}$$

$$\boldsymbol{\nabla}\cdot\mathbf{u} = 0, \tag{2.2}$$

$$\partial_t \mathbf{B} = \boldsymbol{\nabla} \times (\mathbf{u} \times \mathbf{B}) - \frac{1}{R_\mathrm{m}} \boldsymbol{\nabla} \times \left(\frac{1}{\sigma_r} \boldsymbol{\nabla} \times \left(\frac{\mathbf{B}}{\mu_r}\right)\right), \tag{2.3}$$

$$\boldsymbol{\nabla}\cdot\mathbf{B} = 0, \tag{2.4}$$

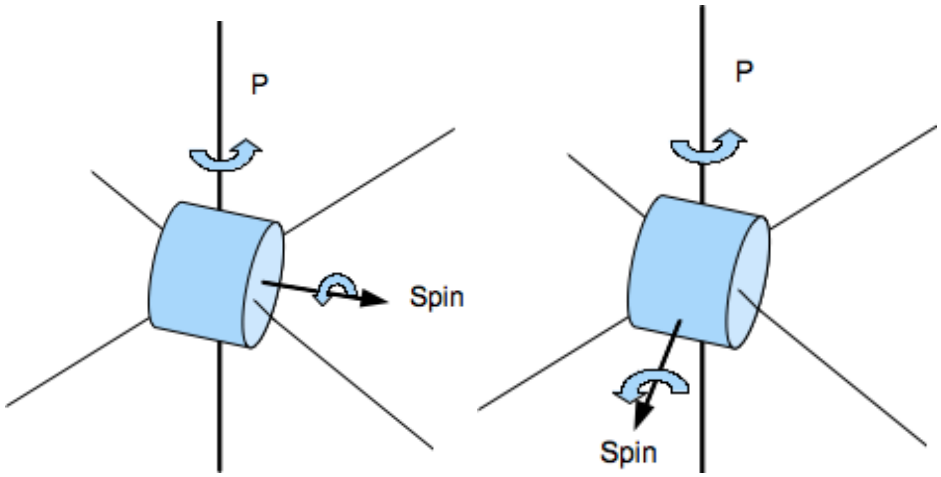

(a) (b)

FIGURE 1. Schematic representation of the *axial spin* (a) and the *equatorial spin* (b) configurations in the laboratory frame.

where $\mathbf{u}$, p, and $\mathbf{B}$ are the velocity field, the reduced pressure including the centrifugal term, and the induction field, respectively, and σ_r and μ_r are the relative conductivity and permeability of the various materials. The spin axis coincides with the symmetry axis i.e., $\mathbf{e}_s = \mathbf{e}_z$ and the precession axis $\mathbf{e}_p = \mathbf{e}_x$ is fixed in the precession frame. The term depending on ε on the left-hand side of (2.1) is the Coriolis acceleration. The no-slip boundary condition on the velocity field is written as follows in the precession frame of reference: $\mathbf{u}_{|\partial\mathcal{C}} = r\mathbf{e}_\theta$, i.e., $\mathbf{u} = \mathbf{e}_\theta$ at $r = 1$ and $\mathbf{u} = r\mathbf{e}_\theta$ at $z = \pm 1$.

To avoid dealing with moving boundaries in the *equatorial spin* case, the computations are performed in the reference frame of the walls of the container (henceforth called the *mantle* frame); the momentum equation is then written as follows:

$$\partial_t \mathbf{u} + (\mathbf{u}\cdot\nabla)\mathbf{u} + 2\mathbf{\Omega}(t)\times\mathbf{u} + \boldsymbol{\nabla} p = \frac{1}{R_\mathrm{e}}\Delta\mathbf{u} + \left[\boldsymbol{\nabla}\times\left(\frac{\mathbf{B}}{\mu_r}\right)\right]\times\mathbf{B} - \frac{d\mathbf{\Omega}}{dt}\times\mathbf{r}. \tag{2.5}$$

where $\mathbf{e}_s = \mathbf{e}_x$ is fixed in this frame and $\mathbf{e}_p$ rotates around $\mathbf{e}_s$. Hence, the Coriolis acceleration on the left-hand side depends on the total angular velocity $\mathbf{\Omega}(t) = \mathbf{e}_x + \varepsilon\mathbf{e}_p(t) = \mathbf{e}_x + \varepsilon(\sin(t)\mathbf{e}_y + \cos(t)\mathbf{e}_z)$ and the term $-\frac{d\mathbf{\Omega}}{dt}\times\mathbf{r}$ on the right-hand side is the so-called Poincaré force. The no-slip boundary condition on the velocity field is written $\mathbf{u}_{|\partial\mathcal{C}} = 0$, i.e., $\mathbf{u} = 0$ at $r = 1$ and $\mathbf{u} = 0$ at $z = \pm 1$.

3. Hydrodynamic study

In this section we examine the above two configurations in the hydrodynamic regime, i.e., we set $\mathbf{B} = 0$. The only control parameter is R_e. At low Reynolds number, the flow is centro-symmetric for both cases, meaning that $\mathbf{u}(\mathbf{r}, t) = -\mathbf{u}(-\mathbf{r}, t)$; it is steady for the axial spin case and it is unsteady for the equatorial spin case. Loss of centro-symmetry is observed at large Reynolds numbers. The loss of centro-symmetry is monitored by inspecting the symmetric and antisymmetric components of the velocity field: $\mathbf{u}_s(r, t) = \frac{1}{2}(\mathbf{u}(\mathbf{r}, t) - \mathbf{u}(-\mathbf{r}, t))$ and $\mathbf{u}_a(\mathbf{r}, t) =$

$\frac{1}{2}(\mathbf{u}(\mathbf{r},t)+\mathbf{u}(-\mathbf{r},t))$. All the computations have been done on centro-symmetric grids, but centro-symmetry has not been otherwise enforced.

3.1. **Energy scaling with Reynolds number in the axial spin case.** We solve equations (2.1)-(2.2) with $\mathbf{B}=0$ for the axial spin case. Recall that the computations for this configuration are done in the precession frame. We start our investigations with a Navier-Stokes run at $R_\mathrm{e}=1200$ as in [10]. The initial velocity field in the precessing frame is the solid body rotation: $\mathbf{u}_0=\mathbf{e}_z\times\mathbf{r}$. The axial circulation induced by precession is monitored by recording the time evolution of the normalized total kinetic energy $K(t)=\frac{1}{2}\int_\mathcal{C}\mathbf{u}^2(\mathbf{r},t)\,\mathrm{d}V/K_0$, where $K_0=\frac{1}{2}\int_\mathcal{C}\mathbf{u}_0^2\,\mathrm{d}V$ is the kinetic energy of the initial solid body rotation. This computation is the same as in [10], where it was shown that the time evolution of the total kinetic energy exhibits doubly periodic oscillations. To enrich the dynamics we increase the Reynolds number as reported in figure 2. To save computing time, we restart computations at higher R_e by using velocity fields obtained at smaller R_e. Note that the rotation period is 2π in our units. Surprisingly the time-averaged kinetic energy of the flow decreases with the forcing intensity (characterized by R_e at ε fixed).

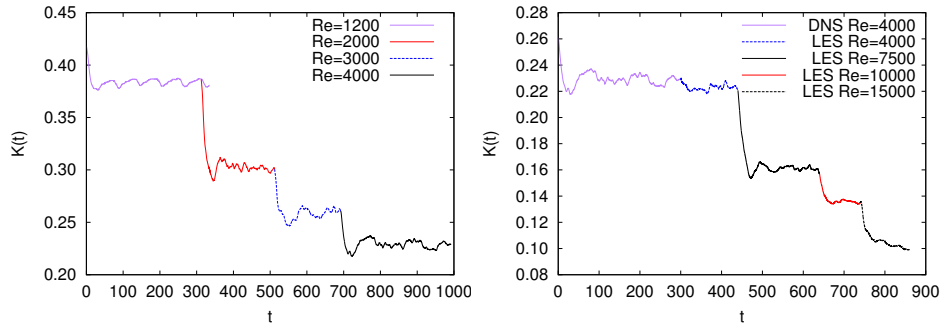

(a) (b)

FIGURE 2. (Color online) Time evolution of the total kinetic energy $K(t)$ in the precession frame for different Reynolds numbers as indicated: (a) DNS at $R_\mathrm{e}=1200, 2000, 3000, 4000$; (b) DNS computation at $R_\mathrm{e}=4000$ and LES computations at $R_\mathrm{e}=4000, 7500, 10000, 15000$.

We perform Direct Numerical Simulations (DNS) for $R_\mathrm{e}\leq 4000$, and we use a stabilization method with similar spatial and time resolution for $R_\mathrm{e}\geq 4000$, (see appendix §A.2 for details on this method). The parameters for the stabilization method (LES in short) are tuned on at $R_\mathrm{e}=4000$. Figure 2b shows the kinetic energy computed with DNS at $R_\mathrm{e}=4000$ for $0\leq t\leq 300$ (same results as in figure 2a shifted in time); the results for $300\leq t\leq 430$ are obtained with LES at $R_\mathrm{e}=4000$. The dynamical behaviour of both simulations is similar; this computation validates our LES technique and the chosen stabilization constants which are henceforth kept constant at higher R_e numbers.

The range of Reynolds numbers that we have explored using our LES method is wide enough to suggest a scaling law for the time-averaged kinetic energy, K,

as a function of the Reynolds number R_e for the precession rate $\varepsilon = 0.15$. To substantiate this claim we show in figure 3a the time-averaged kinetic energy K as a function of R_e. Values for $R_\mathrm{e} < 1200$ are extracted from our previous article [10]. The log-log representation of the data suggests that the energy scales like $K \simeq {R_\mathrm{e}}^{-0.48}$ in the range $R_\mathrm{e} \in [400, 15000]$ (see figure 3b), which in turn suggests the following scaling law for the temporally averaged velocity $\overline{u} \simeq {R_\mathrm{e}}^{-1/4} = {E_\mathrm{k}}^{1/4}$ (where E_k is the Ekman number). This scaling predicts that the average flow vanishes at large R_e in the precession frame. Therefore it should be a solid body motion about the rotation axis in the mantle frame with angular velocity $\mathbf{\Omega} = -\mathbf{e}_z$ (it is a counter-rotation with respect to the spin rotation).

The vanishing of the velocity in the precession frame has been observed in the ATER experiment [7]. The nearly rigid-body rotation in the mantle frame has been discussed in [12], where it is called geostrophic flow. It is shown therein that both the amplitude and the volume occupied by the geostrophic flow grow gradually as ε increases from 0.075 to 0.25 at $R_\mathrm{e} = 2523$, see e.g. [12, Fig.4(a)] (at $R_\mathrm{e} = 10^4$ in the units from [12]).

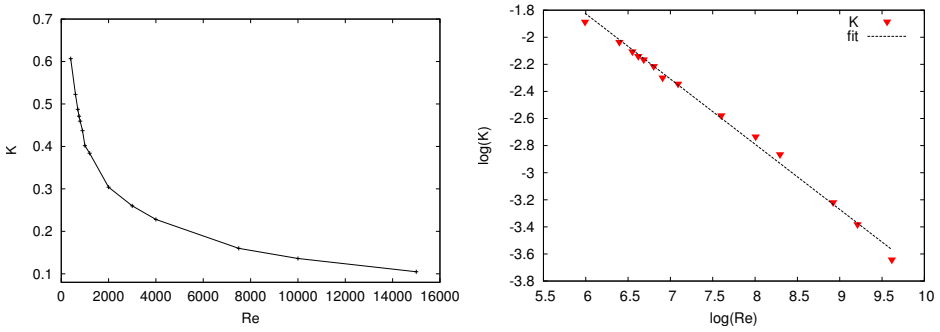

(a) (b)

FIGURE 3. (Color online) Total (time-averaged) kinetic energy K in the precession frame as a function of the Reynolds number R_e: (a) in linear scale and (b) in log-log scale with the fit ${R_\mathrm{e}}^{-0.48}$.

The Poincaré number being fixed $\varepsilon = 0.15$, it is possible to verify whether the global energy damping is uniform when the Reynolds number increases by inspecting the velocity at sample points in the computational domain. The three velocity components, averaged in time and in azimuth, at 9 grid points are shown in Table 3 in the appendix §A.3 for $R_\mathrm{e} = 1200$ and $R_\mathrm{e} = 4000$. All the velocity components are small compared to the wall speed, and the amplitude of most of them indeed diminishes when R_e increases.

More graphic representations are needed to follow other flow features. For instance, figure 4 shows the formation of boundary layers as R_e increases; the highest values of the axial velocity are more and more localized near the lateral wall as R_e grows. The central part of the flow is nearly static and all the small scales, highly intermittent, are pushed towards the wall.

For all the Reynolds numbers, we observe a central S-shaped vortex deformed by the precession and connected to the walls through viscous boundary layers (see

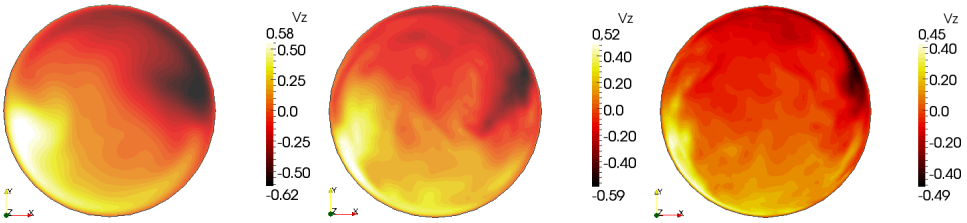

(a) (b) (c)

FIGURE 4. (Color online) Snapshots of contours of the axial velocity in the equatorial plane in the precession frame: (a) at $t = 302$ and $R_e = 1200$, (b) at $t = 235$ and $R_e = 4000$ and (c) at $t = 850$ and $R_e = 15000$.

figure 5). The vorticity lines are more entangled and the central part of the vortex is more aligned with the x-axis (the precession axis) as R_e increases.

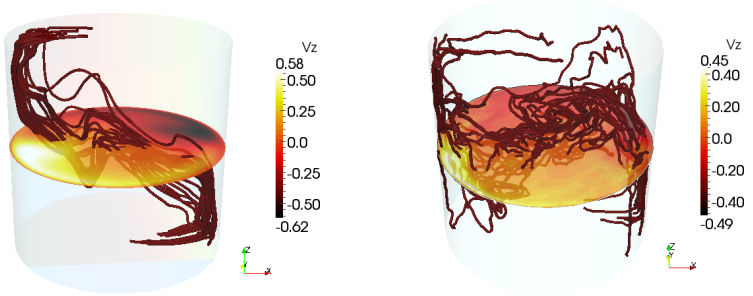

(a) (b)

FIGURE 5. (Color online) Streamlines of the instantaneous vorticity field (in red/dark grey) from a perspective point of view and contours of the axial velocity in the equatorial plane: (a) $R_e = 1200$ and (b) $R_e = 15000$.

The tendency to alignment with the precession axis is also apparent on the time-averaged velocity and vorticity fields as displayed in figure 6. A similar three-dimensional structure has been observed in [16] in simulations of a precessing sphere in the axial spin case at $\varepsilon = 0.1$ and $R_e = 10^4$. The origin of this structure is attributed therein to a pair of large-scale energetic vortex tubes (see figure 16 in [16]). For a precessing cylinder, this structure is the trace of the S-shape vortex observed at all Reynolds numbers.

We can now interpret the scaling $K \simeq 1/\sqrt{R_e}$ as follows. The wall-localization observed above as $R_e \to +\infty$ suggests that the kinetic energy is concentrated in a small layer of thickness δ on the lateral wall (within the volume $2\pi R\delta H$). Hence $K \simeq \pi R(\Omega R)^2 \delta H$ gives $\delta/R \approx 1/\sqrt{R_e}$, which is reminiscent of the usual thickness of a viscous boundary layer.

3.2. **Equatorial spin forcing.** We solve (2.5) with $\mathbf{B} = 0$ for the equatorial spin case. Recall that the computations for this configuration are done in the mantle

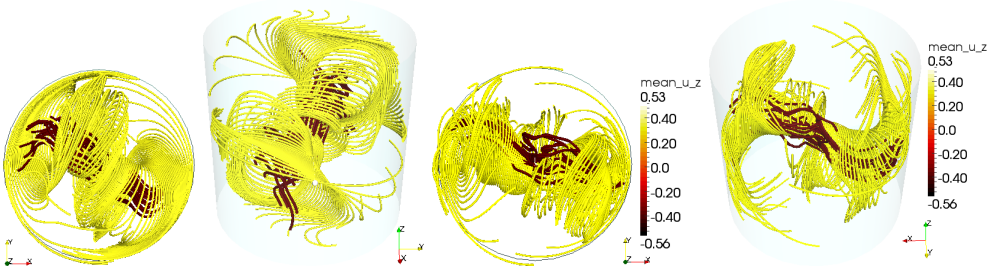

(a) top view, 1200 (b) side view, 1200 (c) top view, 4000 (d) side view, 4000

FIGURE 6. (Color online) Streamlines of the mean velocity field (in yellow/light grey) and of the mean vorticity field (in red/dark grey) in the precession frame. Illustrated are 100 streamlines for $\mathbf{u}$ with endpoints distributed uniformly on the Ox axis and 20 streamlines for $\boldsymbol{\nabla}\times\mathbf{u}$ with endpoints distributed uniformly on a sphere of radius 0.2: (a-b) $R_\mathrm{e} = 1200$ and (c-d) $R_\mathrm{e} = 4000$.

frame. We now normalize the total kinetic energy by the kinetic energy of the solid rotation about the equatorial axis $\mathbf{e}_x$. We set $E_0^\perp = \frac{1}{2}\int_\mathcal{C}(\mathbf{u}_0^\perp)^2\,\mathrm{d}V$, where $\mathbf{u}_0^\perp = \mathbf{e}_x\times\mathbf{r}$, and we define the normalized total kinetic energy in the mantle frame $E^\perp(t) := \frac{1}{2}\int_\mathcal{C}\mathbf{u}^2\,\mathrm{d}V/E_0^\perp$, the asymmetric kinetic energy $E_a^\perp(t) := \frac{1}{2}\int_\mathcal{C}\mathbf{u}_a^2\,\mathrm{d}V/E_0^\perp$ and the asymmetry ratio $r_a^\perp(t) := E_a^\perp(t)/E^\perp(t)$.

Figure 7a shows the time evolution of the total kinetic energy in the mantle frame. The kinetic energy rapidly increases with R_e for moderate Reynolds numbers and then seems to saturate at large Reynolds numbers. The time evolution of the asymmetry ratio is shown in figure 7b for three different Reynolds numbers. The asymmetry ratio fluctuates in time and the flow is clearly asymmetric for $R_\mathrm{e} \geq 1000$. The asymmetry ratio seems to saturate around 6% at large Reynolds numbers.

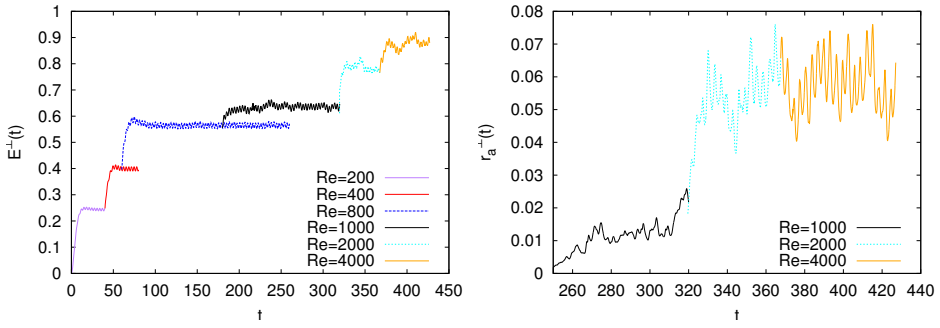

(a) (b)

FIGURE 7. (Color online) Time evolution of (a) the total kinetic energy $E^\perp(t)$ and (b) the asymmetry ratio $r_a^\perp(t) = E_a^\perp(t)/E^\perp(t)$ in the mantle frame at different Reynolds numbers R_e in the equatorial spin case.

3.3. **Comparison between equatorial and axial spin forcing.** In order to compare the efficiency of the energy injection of the two precession techniques we perform a change of reference frame for the axial spin case. Let $\mathbf{u}(\mathbf{r},t)$ be the velocity field obtained in the axial spin case, we then define $\mathbf{u}^{\parallel}(\mathbf{r},t) := \mathbf{u}(\mathbf{r},t) - \mathbf{e}_z \times \mathbf{r}$. The field $\mathbf{u}^{\parallel}(\mathbf{r},t)$ is the mantle frame representation of the velocity field obtained in the axial spin case. It is now reasonable to compare $\mathbf{u}^{\parallel}(\mathbf{r},t)$ with the velocity field obtained in the equatorial spin case, since both fields are represented in the mantle frame. We consequently define $E^{\parallel} = \frac{1}{2}\int_{\mathcal{C}} (\mathbf{u}^{\parallel})^2 \, \mathrm{d}V/K_0$, this choice of normalization will become clear below. Note that the normalization of $E^{\parallel}$ and K is the same, but $E^{\parallel}$ and $E^{\perp}$ are normalized differently. To summarize, $E^{\parallel}$ is the normalized kinetic energy in the mantle frame for the axial spin case and $E^{\perp}$ is the normalized kinetic energy in the mantle frame for the equatorial spin case. For example, we display the time evolution of the kinetic energy of the axial spin case at $R_\mathrm{e} = 1200$ in the two reference frames in figure 8a.

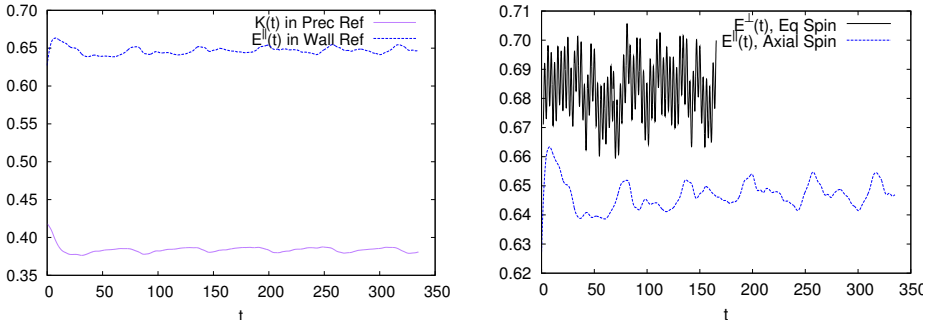

(a) Axial spin case at $R_\mathrm{e} = 1200$ recorded in the two frames

(b) Axial and equatorial spin cases in the mantle frame

FIGURE 8. (Color online) (a) Time evolution at $R_\mathrm{e} = 1200$ of the kinetic energy $K(t)$ in the precession frame as in figure 2a and of the transformed kinetic energy $E^{\parallel}(t)$ in the mantle frame for the axial spin case. (b) Comparison of the kinetic energy in the mantle frame for the axial and the equatorial spin cases at $R_\mathrm{e} = 1200$.

We plot in figure 8b the normalized kinetic energy of the two configurations in the mantle frame at $R_\mathrm{e} = 1200$. Note that both the time-averaged value of the kinetic energy and the fluctutations are larger in the equatorial spin case than in the axial spin case.

We show in figure 9a the spectrum of K (axial forcing) and $E^{\perp}$ (equatorial forcing) with respect to the azimuthal Fourier modes at some time. The computations are done at Reynolds number $R_\mathrm{e} = 1200$. Note that the equatorial spin case needs twice Fourier modes as much as the axial spin case, therefore the computations are more demanding. We show in figures 9b and 9c snapshots of instantaneous vorticity and velocity fields in the precession frame for the axial spin case and in the mantle frame for the equatorial spin case. We observe different features in the two flows: the spin axis case displays a deformed S-shape vortex approximately contained in a meridian plane and the velocity field is localized near the side wall; the equatorial

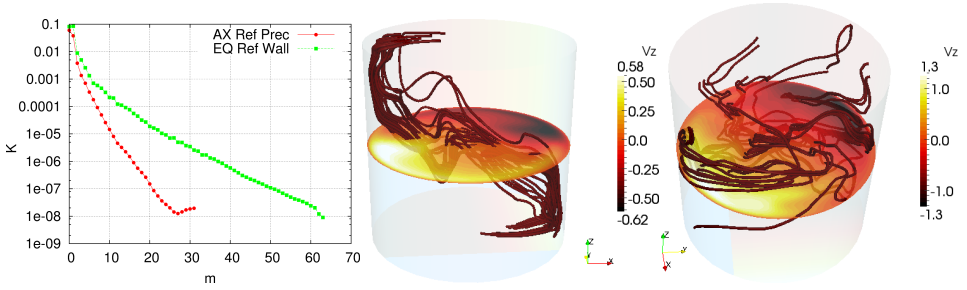

(a) Energy spectra (b) axial spin case (c) equatorial spin case

FIGURE 9. (Color on line) Comparison between the axial and equatorial spin cases: kinetic energy azimuthal spectra as a function of the azimuthal mode m (a) and snapshot at $R_e = 1200$ of the vorticity field lines (red/dark grey) and contours of the axial velocity component in the equatorial plane: (b) axial spin case (same as figure 5a in the precession frame), (c) equatorial spin case (in the mantle frame).

spin case shows no coherent vortical structure, and the small-scales of the velocity are localized near the wall.

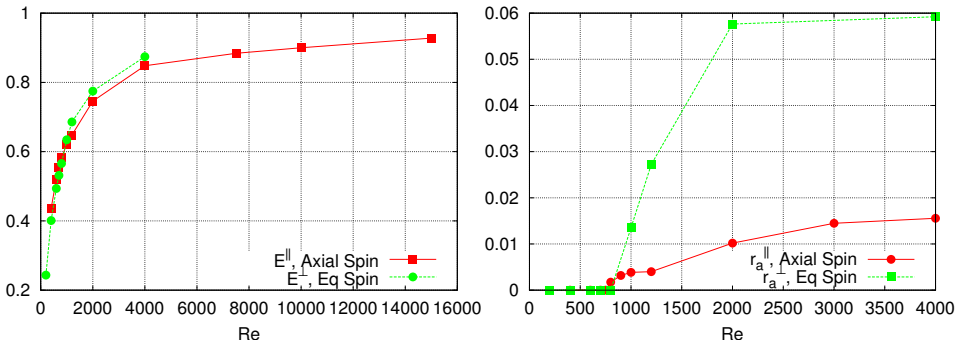

(a) (b)

FIGURE 10. (Color on line) Comparisons between the axial and equatorial spin cases in the mantle frame: (a) time-averaged kinetic energy $E^{\parallel}$ and $E^{\perp}$ as a function of R_e; (b) time-averaged asymmetry ratio $E_a^{\parallel}/E^{\parallel}$ and $E_a^{\perp}/E^{\perp}$ as a function of R_e.

We compare in figure 10a the time-averaged values of the total kinetic energies $E^{\parallel}$, $E^{\perp}$ as a function of R_e. We have seen in §3.1 that at large R_e the velocity (in the axial spin case) in the mantle frame tends to a nearly rigid body rotation about the spin axis $\mathbf{e}_z$. The normalized time-averaged kinetic energy $E^{\parallel}$ approaches the value 1 in this frame, (whence the normalization by K_0 chosen above). In the laboratory frame, this motion corresponds to a nearly rigid rotation about the static precession axis. In the equatorial spin case, we observe that the kinetic energy $E^{\perp}$ (computed in the mantle frame) seems also to converge to the value 1. An easy way

to visualize the flow in the mantle frame is to choose the meridian plane ($x = 0$) orthogonal to the spin axis. Figure 11 shows the velocity field for $R_e = 1200$ and $R_e = 4000$ at two arbitrary times in the meridian section ($x = 0$). Although the boundary conditions require that the velocity vanishes on the container walls, we observe that the flow speed is maximal close to the walls and even exceeds the wall speed in the inertial frame. The cylinder spins counter-clockwise about the x-axis, but the rotation of the bulk flow appears to be clockwise in the ($x = 0$) plane, meaning that the viscous and pressure forces exerted by the moving walls fail to drive the fluid at the spin rate. This fact has already been observed in the ATER experiment [7] at much higher R_e. The green isoline $u_x = 0$ crosses the meridian plane, showing a clear spatial separation between positive and negative values, which suggests that the flow undergoes in the mantle frame a global rotation around an axis roughly coinciding with the isoline $u_x = 0$. We have verified that this line rotates with time approximately at angular velocity $\Omega = -\mathbf{e}_x$ in the plane (Oy, Oz) (data not shown), as does the precession axis. The exact position of the precession axis depends on the initial phase at the beginning of each simulation.

These pictures confirm that at $\varepsilon = 0.15$ and for both driving cases, when R_e is large enough, the flow in the mantle frame experiences a nearly solid body rotation around the spin axis with an angular velocity opposite to the spinning angular velocity; therefore in the laboratory frame, the largest scales of the flow are close to a nearly solid body rotation around the precession axis.

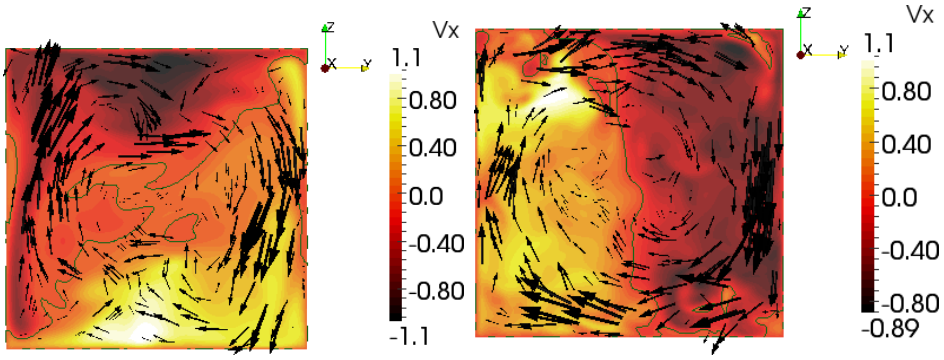

(a) $R_e = 1200$ (b) $R_e = 4000$

FIGURE 11. (Color on line) Equatorial spin case: flow in the mantle frame, in the meridian plane ($x = 0$) orthogonal to the spin axis, at $R_e = 1200$ and $R_e = 4000$. The black arrows represent the 2D velocity field (u_y, u_z) in the plane $(x = 0)$, and the contour levels show the u_x component in this plane. The green line shows the contour level $u_x = 0$.

There are however important differences between the flows induced by the two forcings. For example, the centro-symmetry is lost at $R_e \gtrsim 800$ in both cases but the asymmetry ratio increases faster in the equatorial spin case than in the axial spin case; the ratio $r_a^{\perp}/r_a^{\parallel}$ is larger than three at large Reynolds numbers (see figure 10b). The equatorial spin case is therefore more efficient in breaking the centro-symmetry than the axial spin case.

We finally propose to take another perspective on this problem by looking at the time-averaged flows over several turns. Figure 12 shows the time-averaged velocity and vorticity fields at $R_e = 1200$ for the axial and equatorial spin cases. This figure reveals a rather structured large-scale flow for the axial spin case while no coherent feature is apparent in the equatorial spin case.

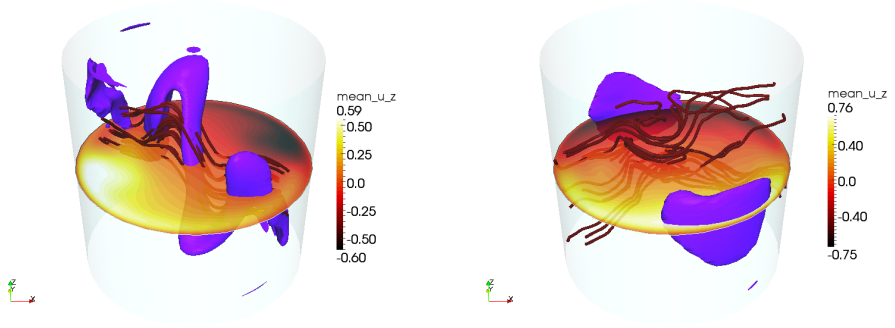

(a) axial spin (b) equatorial spin

FIGURE 12. (Color on line) Time-averaged velocity field at $R_e = 1200$ for the axial and equatorial spin cases: vorticity field lines (red/dark grey), contours of the axial velocity component in the equatorial plane and isosurface of $|\mathbf{u}|^2$: (a) axial spin case (with $|\mathbf{u}|^2$ at 0.3% of maximum in the precession frame), (b) equatorial spin case (with $|\mathbf{u}|^2$ at 70% of maximum in the mantle frame).

Based on the phenomenological argument that dynamo action is favored by symmetry breaking, it could be anticipated from the above observations that the equatorial spin case would generate dynamo action at a lower threshold than the axial spin case. However, it is shown in section 4.2 that this intuitive argument is incorrect.

4. Dynamo action

We now investigate the MHD regime, where R_e and R_m are the two control parameters. The nonlinear MHD simulations use a small magnetic seed field as initial data or restart from a state computed at neighboring parameters. As already observed for spherical and spheroidal dynamos, dynamo action occurs after symmetry breaking of the flow when the magnetic dissipation is small enough, i.e. for magnetic Reynolds numbers R_m above a critical value $R_m^c(R_e)$.

4.1. **Axial spin case.**

4.1.1. *Reminder from* [10]. In [10], we have explored a large range of the kinetic and magnetic Reynolds numbers and found dynamo action for $R_e = 1200$ and $R_m \geq R_m^c \approx 775$ when the solid walls of the vessel are assumed to be insulating. The growing magnetic field that is observed rotates in the precession frame of reference and is dominated by the $m = 2$ mode: as shown in figure 13b, the magnetic field lines show a mainly quadrupolar structure in the vacuum when seen from the top of the cylinder.

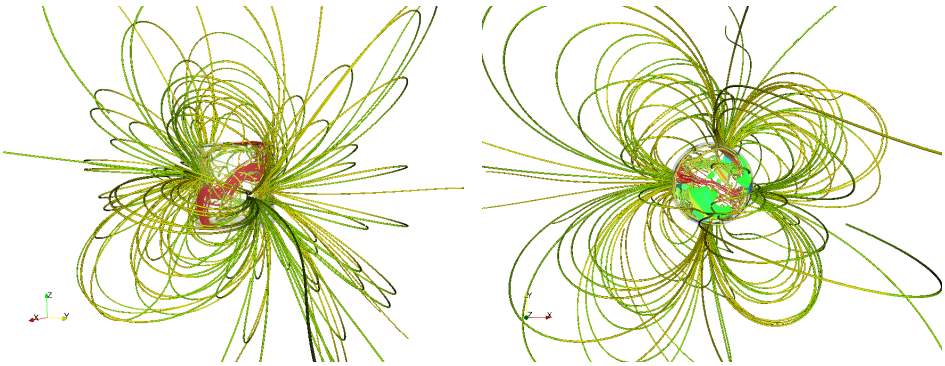

(a) 'insulating' case in perspective (b) 'insulating' case from the top

FIGURE 13. Snapshot at $R_e = 1200$, $R_m = 2400$ for the 'insulating' case showing vorticity field lines (red lines inside the cylinder) and magnetic field lines colored by the axial component [yellow (green) for positive (negative) h_z component]: (a) perspective view, (b) from the top of the cylinder (in the precession frame). From [10].

We now present in the rest of this section new results obtained when using conducting or ferromagnetic walls of relative thickness $w = 0.1$ at different places. The relative conductivity of these additional walls is chosen to be that of copper i.e., $\sigma_r = 4.5$ (and $\mu_r = 1$) or the relative magnetic permeability is taken to be that of soft iron [17], i.e., $\mu_r = 65$ (and $\sigma_r = 1$).

4.1.2. *Numerical results with thick conducting walls.* We study the influence of the conducting walls with $\sigma_r = 4.5$ and $\mu_r = 1$. We keep $R_e = 1200$ and vary R_m to find the dynamo threshold, i.e., when the growth rate of the magnetic energy is zero. We define four cases as follows. We call 'insulating' case the configuration studied in [10], the 'side' case corresponds to adding conducting walls on the cylindrical side of the vessel, the 'lid' case corresponds to adding conducting walls at the top and bottom of the vessel, and the 'wall' case corresponds to adding conducting walls everywhere.

We first show in figure 14a a series of dynamo simulations done with $R_m = 300, 400$ and 900 for the 'side' case. The figure shows the time evolution of the magnetic energy $M(t) = \int_{\Omega_c} \frac{1}{2}\mathbf{B}^2/\mu_0\mu_r dV$ where Ω_c is composed of the fluid domain and the walls. We start the $R_m = 900$ run with a magnetic seed and integrate long enough to get a decrease or an increase of M. Dynamo action occurs when $M(t)$ is an increasing function of time as is the case for $R_m = 900$ and $R_m = 400$ but not for $R_m = 300$. The initial velocity and magnetic fields for the runs at $R_m = 400$ are the velocity and the magnetic fields obtained from the run at $R_m = 900$ at time $t = 47$. For $R_m = 300$, we restart from $R_m = 400$ at time $t = 107$. Linear interpolation of the growth rates gives an estimate of the critical magnetic Reynolds number $R_m^c \approx 365$ for the 'side' case.

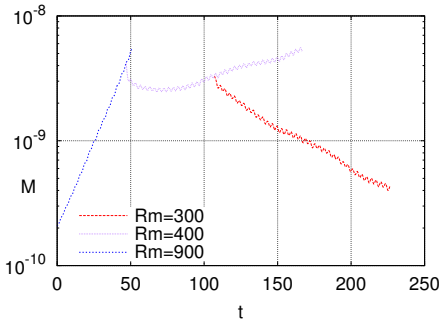

(a) $M(t)$ for the 'side' case

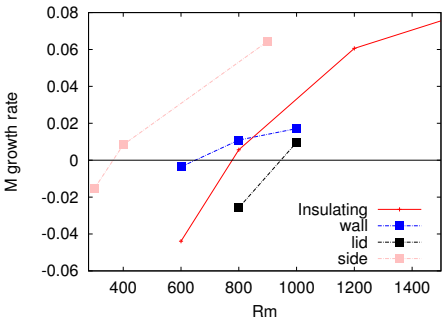

(b) Growth rates vs. R_m

FIGURE 14. Conducting walls: (a) Time evolution of the magnetic energy $M(t)$ in the conducting fluid at $R_\mathrm{e} = 1200$ and various R_m as indicated (in lin-log scale) for the 'side' case; (b) Growth rates of the magnetic field energy as a function of R_m for various configurations. The values are for $R_\mathrm{e} = 1200$ and the thickness of either conducting wall type is taken as $0.1R$, with a relative conductivity $\sigma_r = 4.5$ and relative magnetic permeability $\mu_r = 1$.

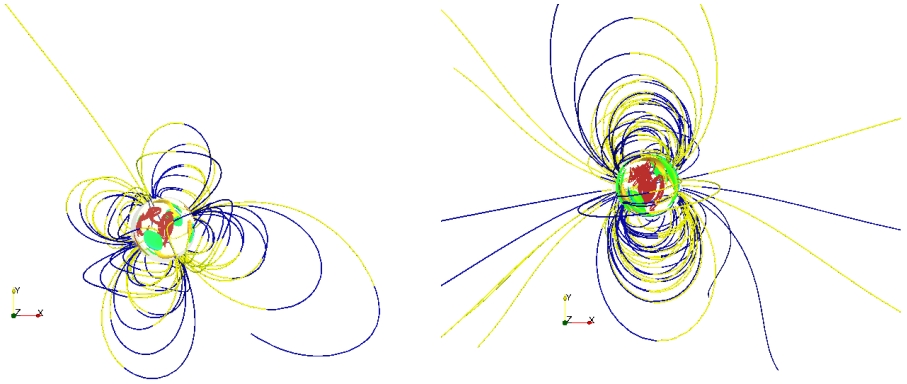

(a) From the top for the 'lid' case

(b) From the top for the 'side' case

FIGURE 15. Conducting walls: Snapshots at (a) $R_\mathrm{e} = 1200$, $R_\mathrm{m} = 1000$ for the 'lid' case and (b) $R_\mathrm{e} = 1200$, $R_\mathrm{m} = 900$ for the 'side' case showing vorticity field lines (red lines inside the cylinder) and magnetic field lines colored by the axial component [yellow (blue) for positive (negative) h_z component].

We perform two other series of simulations and collect the growth rates in figure 14b. The thresholds are $R_\mathrm{m}^c(\text{'side'}) \approx 365 < R_\mathrm{m}^c(\text{'wall'}) \approx 650 < R_\mathrm{m}^c(\text{'insulating'}) \approx 775 < R_\mathrm{m}^c(\text{'lid'}) \approx 965$. We observe that the 'lid' walls are highly detrimental to the dynamo action whereas adding the conducting 'side' walls helps it. This phenomenon is reminiscent to the results found in [18, 19] for the von Kármán Sodium experiment.

Note that when using walls with the same conductivity as the liquid (i.e., $\sigma_r = 1$ as in [20]), the smallest threshold is also obtained for the 'side' case, and the corresponding critical magnetic Reynolds number is $R_{\mathrm{m}}^c \approx 550$. This observation suggests that increasing the conductivity of the side wall reduces the dynamo threshold.

Conducting walls enable currents to loop on longer scales but also lead to different growing magnetic field structures (see figure 15). The 'lid' configuration and the 'insulating' configuration lead to a mainly quadrupolar magnetic field while the 'side' case gives rise to a mainly equatorial dipolar magnetic field. The 'wall' configuration shows an oblique dipolar magnetic field (data not shown).

4.1.3. *Numerical results with thick Ferromagnetic walls.* We now study the influence of the ferromagnetic walls with $\mu_r = 65$ and $\sigma_r = 1$. We keep $R_{\mathrm{e}} = 1200$ and vary R_{m} to find the threshold, i.e., when the growth rate of the magnetic energy is zero. We define four cases as before. We call 'insulating' case the configuration studied in [10], the 'side' case corresponds to adding ferromagnetic walls on the cylindrical side of the vessel, the 'lid' case corresponds to adding ferromagnetic walls at the top and bottom of the vessel, and the 'wall' case corresponds to adding ferromagnetic walls everywhere. We perform linear dynamo simulations and collect the growth rates in figure 16a. The thresholds obtained are $R_{\mathrm{m}}^c(\text{'insulating'}) \approx 775 < R_{\mathrm{m}}^c(\text{'side'}) \approx 800 < R_{\mathrm{m}}^c(\text{'wall'}) \approx 840 < R_{\mathrm{m}}^c(\text{'lid'}) \approx 880$. We observe that adding ferromagnetic walls increases the threshold in all the cases. In the 'wall' case the magnetic energy is dominated by the $m = 1$, 2 modes and the growing magnetic field is an equatorial dipole (see figure 16b).

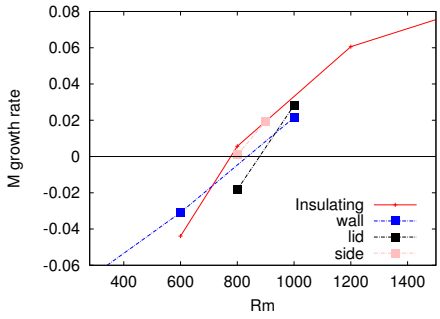

(a) Growth rates vs. R_{m}

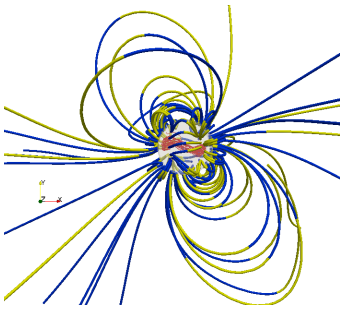

(b) Snapshot for the 'wall' case with $\mu_r = 65$

FIGURE 16. Ferromagnetic walls: (a) Growth rates of the magnetic field energy as a function of R_{m} for various configurations. The values are for $R_{\mathrm{e}} = 1200$ and the thickness of either ferromagnetic wall type is taken as $0.1R$, with a relative conductivity $\sigma_r = 1$ and relative magnetic permeability $\mu_r = 65$. (b) Snapshot at $R_{\mathrm{e}} = 1200$, $R_{\mathrm{m}} = 1000$ for the 'wall' case showing vorticity field lines (red lines inside the cylinder) and magnetic field lines colored by the axial component [yellow (blue) for positive (negative) h_z component]. View from the top.

Although a predictive explanation of the dependence on σ_r and μ_r of the dynamo threshold is still lacking at the present time, the impact of the nature of the walls

seems crucial for the design of experimental fluid dynamos. For conducting walls, the increase of R_{m}^{c} from the 'side' case to the 'lid' case suggests to diminish the influence of the lid by lowering its conductivity: for example, it would be interesting to consider an inner lateral copper layer attached to the outer stainless steel shell of the dynamo vessel in the DRESDYN precession experiment. In any configuration ferromagnetic walls seem to be detrimental to the dynamo action.

4.2. **Equatorial spin case.** We now want to test if the equatorial spin case with a higher level of asymmetric energy is more efficient for dynamo action than the axial case. For that purpose, various MHD runs are performed at $R_{\mathrm{e}} = 1200$ for different values of the magnetic Reynolds numbers R_{m} as in [10]. The onset of dynamo action is monitored by recording the time evolution of the magnetic energy in the conducting fluid, $M(t)$. Two types of simulations are done: linear dynamo runs are first performed by imposing $\mathbf{B} = 0$ in equation (2.5), i.e., the retroaction of the Lorentz force on the velocity field is disabled; then the Lorentz force is restored to observe the nonlinear saturation and the full system of equations (2.2),(2.3),(2.4),(2.5) is solved.

4.2.1. *Linear regime.* A first series of linear dynamo simulations is done with $R_{\mathrm{m}} = 1200, 2000$ and 2400. The time evolution of $M(t)$ is shown in figure 17a. The initial velocity field and magnetic field for the runs at $R_{\mathrm{m}} = 2000$ and 2400 are the velocity and the magnetic fields obtained from the run at $R_{\mathrm{m}} = 1200$ at time $t = 282$. Dynamo action is declared to occur when $M(t)$ is an increasing function of time for large times with a positive growthrate (as is the case for $R_{\mathrm{m}} = 2400$). Linear interpolation of the growthrates gives the critical magnetic Reynolds number $R_{\mathrm{m}}^{c} \approx 2130$ at $R_{\mathrm{e}} = 1200$, i.e., the critical magnetic Reynolds number is almost three times larger than that in the axial spin case (see section 4.1.1).

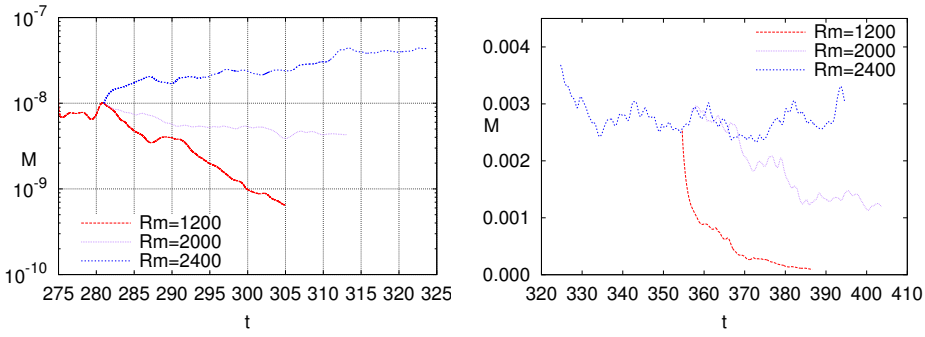

(a) $M(t)$ in linear regime

(b) $M(t)$ in nonlinear regime

FIGURE 17. Equatorial spin case: Time evolution of the magnetic energy $M(t)$ in the conducting fluid (a) in the linear regime from $t = 275$ at $R_{\mathrm{e}} = 1200$ and various R_{m} as indicated (in lin-log scale) and (b) in the nonlinear regime.

4.2.2. *Nonlinear regime.* To observe the nonlinear saturation, we use as initial data the velocity and magnetic fields from the linear MHD run at $t = 323$ for $R_{\mathrm{m}} = 2400$ (see figure 17a). The amplitude of the initial magnetic field is multiplied arbitrarily

by 200 to reach saturation faster; the initial velocity field is kept unchanged. Figure 17b shows that $M(t)$ decreases rapidly over a time period corresponding to one turnover time, i.e., until $t = 329$, and begins to oscillate thereafter. After restarting the MHD run at $t = 357$ with $R_{\rm m} = 2000$ and running it until $t = 405$, we observe that $M(t)$ decreases with time. After restarting the MHD run at $t = 355$ with $R_{\rm m} = 1200$ and running it until $t = 387$, we observe that the dynamo dies in a short time lapse. A snapshot of the vorticity and the magnetic field lines at $R_{\rm e} = 1200$ and $R_{\rm m} = 2400$ is shown on figure 18. Vortex lines are connected to the walls through viscous boundary layers. The magnetic energy is dominated by the azimuthal modes $m = 1, 2, 3$ and the magnetic field lines exhibit a complex shape.

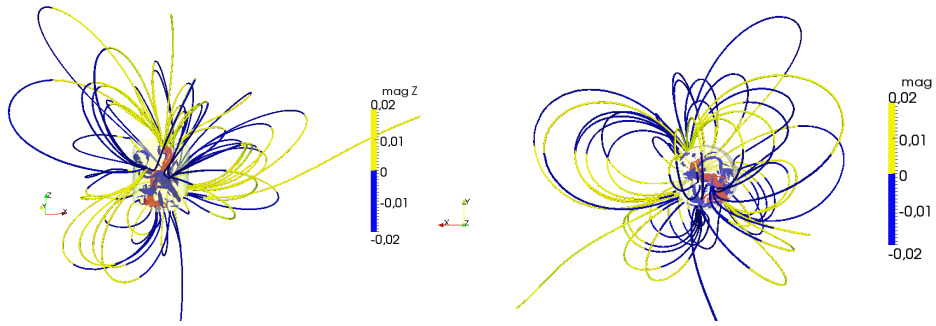

(a) from the side (b) from the top

FIGURE 18. (Color on line) Equatorial spin case: snapshot in the mantle frame at $t = 395$ at $R_{\rm e} = 1200$ and $R_{\rm m} = 2400$ of the vorticity field lines (grey/red) and the magnetic field lines colored by the axial component (light grey/yellow for positive axial magnetic field component and black/blue for negative axial magnetic field component). (a) The view is seen from the side (Ox is the spin axis, Oz the precession axis), (b) from the top.

5. Conclusion

Using numerical simulations, we have extended the scope of precession forcing in hydrodynamic and magnetohydrodynamic regimes by assuming that the symmetry axis of a cylindrical container does not coincide necessarily with the spin axis. To reduce the parameter space, we have fixed the Poincaré number, the ratio of precession to spin rotation, to $\varepsilon = 0.15$, and we have chosen a container length equal to its diameter. We have considered equatorial spin forcing besides the more conventional axial spin case, with a spin axis orthogonal to the precession axis. In the axial spin case, the kinetic energy in the precession frame decreases when the Reynolds number increases. The kinetic energy scales like ${R_{\rm e}}^{-0.48}$, which suggests that the most energetic scales are concentrated in a viscous boundary layer. Thus the conclusion of the numerical simulations that there is inhibition of the spin motion is in agreement with the experimental observations [7] made at Reynolds numbers hundred times larger than the ones computed in the present paper. In the precession frame, the azimuthal speed decreases rapidly from the wall in the viscous

boundary layer, while a 3D bulk flow involving axial velocities is formed. In the mantle frame, kinetic energy appears to increase with the Reynolds number, since the bulk flow is nearly in counter-rotation with respect to the container frame.

Using equatorial spin forcing, the kinetic energy increases with the Reynolds number in the mantle frame, indicating that the flow also tends to the rotation opposite to the spin motion. This fact suggests that the precession acts efficiently against the inertial forcing by the moving walls. At $R_e = 4000$, for example, the kinetic energy is close to 90% of that of the solid body spin motion.

The inhibition of the flow spin may be explained as the consequence of an alternating spin direction: at two moments separated by a half period of precession, the directions of the container spin are opposite in the laboratory frame. While nobody would be surprized that a purely oscillating spin leads to no mean flow motion, we have confirmed that the same result carries over for the two limit spin angles, with a precession rate of 0.15 and $R_e \leq 15000$. This picture suggests a more general conjecture, to be verified numerically and experimentally for any container geometry: for a sufficient effective Poincaré number (equal to the perpendicular projection of the precession frequency w.r.t. the spin axis) and in the limit of large Reynolds numbers, the precession forcing leads to a solid body rotation in the bulk flow, with a concentration of viscous dissipation in the boundary layers.

In the perspective of dynamo action, the asymmetry ratio saturates at rather low values, although different in the axial spin case (around 1.8%) and in the equatorial spin case (around 6%). Contrary to what could be expected from these results, the critical magnetic Reynolds number is found to be lower for the axial spin configuration than for the equatorial spin case. This result contradicts the intuition that wall-normal stress would enhance symmetry breaking and would favor dynamo action. Inspection of the flows at $R_e = 1200$ reveals different features like more small-scales in the equatorial spin case with a less coherent large-scale flow.

Our results of varying wall properties of a cylinder precessing in the axial spin configuration are encouraging for the optimization of the critical magnetic Reynolds number for the planned experiment at DRESDYN, where magnetic Reynolds numbers as large as 700 are expected to be reached: it could be interesting to add an inner copper layer inside the stainless steel container. The question of self-excitation in a real precession experiment is far from being settled though.

Appendix A

A.1. **SFEMaNS code.** All the hydrodynamic and MHD computations reported in this paper have been done with a code called SFEMaNS. This code uses a hybrid spatial discretization which involves spectral and finite elements. In a nutshell we use a Fourier decomposition in the azimuthal direction such that the problem for each Fourier can be approximated independently (modulo the computations of non-linear terms) for each the meridian plane. We use Hood-Taylor continuous Lagrange elements for the pressure and the velocity, i.e., piecewise linear polynomials for the pressure and piecewise quadratic polynomials for the velocity field. The method is third-order accurate is space for the velocity. For the magnetic part, the algorithm solves the problem using the magnetic induction, $\mathbf{B}$, in the conducting region (after standard elimination of the electric field) and the scalar magnetic potential in the insulating exterior. The fields in each region are approximated by using H^1-conforming Lagrange elements, with a technique to control the divergence of $\mathbf{B}$

in a negative Sobolev norm that guarantees convergence under minimal regularity (see details in [21], [22, §3.2], [23]). The coupling at the conductor/insulator interface is done by using an interior penalty method. SFEMaNS has been thoroughly validated on numerous manufactured solutions and against other MHD codes (see e.g. [24, 25, 26, 27]).

A.2. **Stabilization method.** For Reynolds numbers beyond a few thousands, large gradients, which produce even smaller scales by the action of nonlinearity, are not correctly represented by the mesh due to lack of computational resources. Energy that should have been dissipated accumulates at the grid scale. A stabilization method that handles this problem has been implemented in SFEMaNS. This method, called entropy viscosity, was developed by J.-L. Guermond et al. [28], [29], and consists of adding a local artificial viscosity made proportional to the residual of the kinetic energy equation. This artificial viscosity induces a diffusion proportional to the energy imbalance which allows the unresolved scales to be better accounted for.

Let us now give some technical details on the computation of the entropy viscosity. We consider a mesh $\mathcal{K}_\mathrm{h}$ of the domain composed of a collection of cells K with local mesh-size h_K. We introduce a time-step $\tau > 0$ and set $\phi^n = \phi(n\tau)$ for any time-dependent function ϕ. Then we define the residual of the momentum equation as follows:

$$\mathrm{Res}^n_\mathrm{NS} = \frac{\mathbf{u}^n - \mathbf{u}^{n-2}}{2\tau} + (\mathbf{u}^{n-1}\cdot\boldsymbol{\nabla})\mathbf{u}^{n-1} - \frac{1}{R_\mathrm{e}}\Delta\mathbf{u}^{n-1} + \boldsymbol{\nabla}p^{n-1} - \mathbf{f}^{n-1}, \tag{A.1}$$

where $\mathbf{f}$ takes into account the Coriolis, Poincaré and Lorentz forces depending of the problem setting (axial or equatorial spin cases). This residual is computed at each time step and over every mesh cell. The local artificial viscosity is defined on each cell K by:

$$\nu^n_{R|K} = \frac{h_K^2 \|\mathrm{Res}^n_\mathrm{NS}\cdot\mathbf{u}^n\|_{\mathbf{L}^\infty(K)}}{\|\mathbf{u}^n\|^2_{\mathbf{L}^\infty(\Omega)}}. \tag{A.2}$$

The quantity $\nu^n_{R|K}$ is expected to be as small as the consistency error in smooth regions and to be large in the regions where the PDE is not well resolved. To avoid excessive dissipation and to be able to run with CFL numbers of order $\mathcal{O}(1)$, we define the entropy viscosity as follows:

$$\nu^n_{E|K} = \min\left(c_\mathrm{max} h_K \|\mathbf{u}^n\|_{\mathbf{L}^\infty(K)}, c_\mathrm{e}\nu^n_{R|K}\right), \tag{A.3}$$

where $c_\mathrm{max} \in (0, \frac{1}{2}]$ and $c_\mathrm{e} \in (0, 1]$ are tunable constants. Technical details about the tuning of c_max and c_e are given in section 2.7 of [28]. Thus defined, the entropy viscosity is high-order in smooth regions and is first-order in regions with large gradients.

To illustrate the behavior of the LES method, we compare in figure 19a the kinetic energy from the DNS and LES computations that have been done for the hydrodynamic study of the axial spin case at $R_\mathrm{e} = 4000$, see section §3.1. The relative differences on the kinetic energies of the DNS and LES computation are less than 2%. We show in figure 19b the energy spectrum at final time of the DNS and LES computations at $R_\mathrm{e} = 4000$. It is clear that the entropy viscosity technique reproduces correctly the energy spectrum of the DNS computation, thereby validating our LES approach.

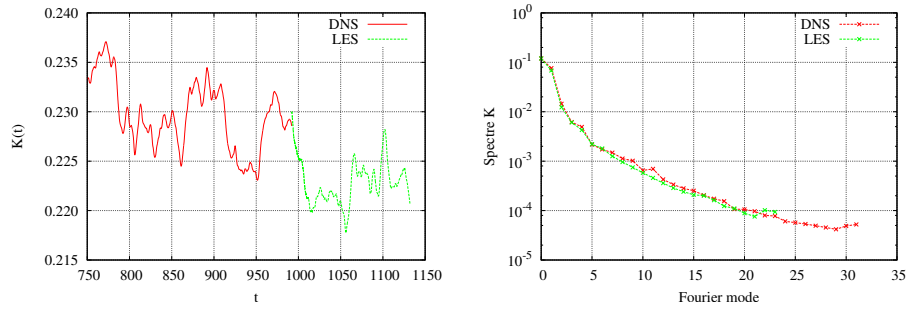

(a) Kinetic energy K (b) Energy spectra at final time

FIGURE 19. Comparisons between DNS and LES results at $R_e = 4000$ in the hydrodynamic regime. (a) Evolution of total kinetic energy $K(t)$ (zoom from figure 2b), (b) kinetic energy spectrum at final time as a function of the Fourier modes ($0 \leq m \leq 31$ with DNS and $0 \leq m \leq 23$ with LES).

For completeness we show in Table 1 the spatial and time resolutions that have been used in the hydrodynamic study of the axial spin case at $R_e \geq 4000$, as reported in Section §3.1. We show also in this table the total CPU time (in hours) on a IBM x3750 for one rotation period, (i.e., wall clock time multiplied by the number of processors used). Note that the MHD runs are a little over 6 times more expensive than the hydrodynamic runs.

R_e	DNS/LES	τ	N_F	h_{bdy}	h_{int}	CPU time
1200	DNS	2.10^{-3}	32	0.0125	0.0125	85
4000	DNS	10^{-3}	32	0.008	0.024	200
4000	LES	10^{-3}	24	0.0125	0.05	40
7500	LES	10^{-3}	32	0.008	0.04	60
10000	LES	10^{-3}	48	0.008	0.04	135
15000	LES	5.10^{-4}	64	0.005	0.02	2800

TABLE 1. Space and time resolutions used for the DNS and LES hydrodynamic computations in the axial spin case. N_F is the number of complex Fourier modes, τ the time step, h_{bdy} the pressure mesh size near the walls of the cylinder and h_{int} the pressure mesh size along the axis $r = 0$ (the velocity field is approximated with **cells twice smaller**). The last column corresponds to the total CPU time on a IBM x3750 (in hours) for one rotation period.

We show in table 2 the typical spatial and time resolutions that have been used in the equatorial spin simulations. The total CPU time (in hours) that is reported corresponds to one rotation period. The computations have been done on a IBM x3750 machine.

R_e	R_m	DNS/LES	τ	N_F	h_{bdy}	h_{int}	CPU time
1200	-	DNS	$7.5\,10^{-4}$	64	0.01	0.02	500
4000	-	LES	3.10^{-4}	64	0.008	0.04	2000
1200	2000	DNS	4.10^{-4}	64	0.01	0.02	1800

TABLE 2. Space and time resolutions used for the DNS and LES computations in the equatorial spin case. When R_m is not indicated, only Navier-Stokes integration is performed. N_F is the number of complex Fourier modes, τ the time step, h_{bdy} the pressure mesh size near the walls of the cylinder and h_{int} the pressure mesh size along the axis $r = 0$ (the velocity field is approximated with **cells twice smaller**). The last column corresponds to the total CPU time on a IBM x3750 (in hours) for one rotation period.

A.3. **Mean velocity components.** We report in Table 3 time and azimuthal averages of the velocity field at various positions in the precession frame for the axial spin case. The computations have been done at $R_e = 1200$ and $R_e = 4000$. We observe that the amplitude of most of the components is small compared to unity, which is the wall speed in the precession frame, and decreases in absolute value when R_e increases. Note the change of sign of the averaged azimuthal velocity when passing from $R_e = 1200$ to $R_e = 4000$.

positions		radial velocity		azimuthal velocity		axial velocity	
z	r	$R_e = 1200$	$R_e = 4000$	$R_e = 1200$	$R_e = 4000$	$R_e = 1200$	$R_e = 4000$
-0.7	0.25	-0.0117	-0.0067	0.0637	-0.0279	-0.1081	0.0010
	0.5	-0.0115	-0.0051	0.0795	-0.0406	-0.0622	-0.0145
	0.75	-0.0075	-0.0031	0.1225	0.0028	0.0050	-0.0094
-0.45	0.25	-0.0278	0.0040	0.0670	-0.0302	-0.0683	0.0059
	0.5	-0.0393	-0.0052	0.0700	-0.0574	-0.0490	-0.0069
	0.75	-0.0330	-0.0078	0.1053	-0.0198	0.0040	-0.0050
0	0.25	-0.0176	-0.0008	0.0815	-0.0515	-0.0007	0.0020
	0.5	-0.0321	0.0044	0.0588	-0.0787	0.0003	-0.0003
	0.75	-0.0307	0.0006	0.0876	-0.0225	0.0003	-0.0014

TABLE 3. Time and azimuthal average of the velocity field at various positions in the precession frame for the axial spin case at two illustrative Reynolds numbers.

ACKNOWLEDGMENTS

The HPC resources for SFEMaNS were provided by GENCI-IDRIS (grant 2015-0254) in France and by the Texas A&M University Brazos HPC cluster. J.-L. Guermond acknowledges support from University Paris Sud, the National Science Foundation, under grant NSF DMS-1015984, DMS-1217262, the Air Force Office of Scientific Research, USAF, under grant/contract number FA9550-15-1-0257, and the Army Research Office under grant/contract number W911NF-15-1-0517.

References

[1] W. V. R. Malkus. Precession of the Earth as the cause of geomagnetism: Experiments lend support to the proposal that precessional torques drive the Earth's dynamo. Science, 160(3825):259–264, 1968.

[2] M. Le Bars, D. Cébron, and P. Le Gal. Flows driven by libration, precession, and tides. Annual Review of Fluid Mechanics, 47(1):163–193, 2015.

[3] F. Stefani, S. Eckert, G. Gerbeth, A. Giesecke, Th. Gundrum, C. Steglich, T. Weier, and B. Wustmann. DRESDYN - a new facility for mhd experiments with liquid sodium. Magnetohydrodynamics, 48:103–113, 2012.

[4] A. Tilgner. Precession driven dynamos. Phys. Fluids, 17(3):034104, 2005.

[5] C.-C. Wu and P. Roberts. On a dynamo driven by topographic precession. Geophys. Astrophys. Fluid Dyn., 103(6):467–501, 2009.

[6] R. F. Gans. On hydromagnetic precession in a cylinder. J. Fluid Mech., 45:111–130, 1970.

[7] W. Mouhali, T. Lehner, J. Léorat, and R. Vitry. Evidence for a cyclonic regime in a precessing cylindrical container. Experiments in Fluids, 53(6):1693–1700, 2012.

[8] R. Lagrange, P. Meunier, F. Nadal, and C. Eloy. Precessional instability of a fluid cylinder. Journal of Fluid Mechanics, 666:104–145, 1 2011.

[9] Y. Lin, J. Noir, and A. Jackson. Experimental study of fluid flows in a precessing cylindrical annulus. Physics of Fluids, 26(4):–, 2014.

[10] C. Nore, J. Léorat, J.-L. Guermond, and F. Luddens. Nonlinear dynamo action in a precessing cylindrical container. Phys. Rev. E, 84:016317, Jul 2011.

[11] D. Kong, X. Liao, and K. Zhang. The sidewall-localized mode in a resonant precessing cylinder. Physics of Fluids, 26(5):–, 2014.

[12] D. Kong, Z. Cui, X. Liao, and K. Zhang. On the transition from the laminar to disordered flow in a precessing spherical-like cylinder. Geophysical & Astrophysical Fluid Dynamics, 109(1):62–83, 2015.

[13] A. Giesecke, T. Albrecht, T. Gundrum, J. Herault, and F. Stefani. Triadic resonances in non-linear simulations of a fluid flow in a precessing cylinder. submitted to New Journal of Physics, arXiv:1508.00334, 2015.

[14] Jianfei Jiang, Dali Kong, Rixiang Zhu, and Keke Zhang. Precessing cylinders at the second and third resonance: Turbulence controlled by geostrophic flow. Phys. Rev. E, 92:033007, Sep 2015.

[15] T. Albrecht, H. M. Blackburn, J. M. Lopez, R. Manasseh, and P. Meunier. Triadic resonances in precessing rapidly rotating cylinder flows. Journal of Fluid Mechanics, 778, 9 2015.

[16] S. Goto, A. Matsunaga, M. Fujiwara, M. Nishioka, S. Kida, M. Yamato, and S. Tsuda. Turbulence driven by precession in spherical and slightly elongated spheroidal cavities. Physics of Fluids, 26(5):–, 2014.

[17] G. Verhille, N. Plihon, M. Bourgoin, Ph. Odier, and J.-F. Pinton. Induction in a von Kármán flow driven by ferromagnetic impellers. New Journal of Physics, 12(3):033006, 2010.

[18] F. Stefani, M. Xu, G. Gerbeth, F. Ravelet, A. Chiffaudel, F. Daviaud, and J. Léorat. Ambivalent effects of added layers on steady kinematic dynamos in cylindrical geometry : application to the VKS experiment. Eur. J. Fluid Mech, B, 25:894, 2006.

[19] R. Laguerre, C. Nore, J. Léorat, and J.-L. Guermond. Effects of conductivity jumps in the envelope of a kinematic dynamo flow. CR Mécanique, 334:593, 2006.

[20] F. Stefani, T. Albrecht, G. Gerbeth, A. Giesecke, T. Gundrum, J. Herault, C. Nore, and C. Steglich. Towards a precession driven dynamo experiment. Magnetohydrodynamics, 51(2):83–92, 2015.

[21] A. Bonito and J.-L. Guermond. Approximation of the eigenvalue problem for the time harmonic Maxwell system by continuous Lagrange finite elements. Math. Comp., 80(276):1887–1910, 2011.

[22] A. Giesecke, C. Nore, F. Stefani, G. Gerbeth, J. Léorat, F. Luddens, and J.-L. Guermond. Electromagnetic induction in non-uniform domains. Geophys. Astrophys. Fluid Dyn., 104(5):505–529, 2010.

[23] A. Bonito, J.-L. Guermond, and F. Luddens. Regularity of the Maxwell equations in heterogeneous media and Lipschitz domains. Journal of Mathematical Analysis and applications, 408(2):498–512, December 2013.

[24] J.-L. Guermond, R. Laguerre, J. Léorat, and C. Nore. An interior penalty Galerkin method for the MHD equations in heterogeneous domains. J. Comput. Phys., 221(1):349–369, 2007.
[25] J.-L. Guermond, R. Laguerre, J. Léorat, and C. Nore. Nonlinear magnetohydrodynamics in axisymmetric heterogeneous domains using a Fourier/finite element technique and an interior penalty method. J. Comput. Phys., 228:2739–2757, 2009.
[26] J.-L. Guermond, J. Léorat, F. Luddens, C. Nore, and A. Ribeiro. Effects of discontinuous magnetic permeability on magnetodynamic problems. J. Comput. Phys., 230:6299–6319, 2011.
[27] A. Giesecke, C. Nore, F. Stefani, G. Gerbeth, J. Léorat, W. Herreman, F. Luddens, and J.-L. Guermond. Influence of high-permeability discs in an axisymmetric model of the Cadarache dynamo experiment. New Journal of Physics, 14(5):053005, 2012.
[28] J.-L. Guermond, R. Pasquetti, and B. Popov. Entropy viscosity method for nonlinear conservation laws. J. Comput. Phys., 230(11):4248–4267, 2011.
[29] J.-L. Guermond, R. Pasquetti, and B. Popov. From suitable weak solutions to entropy viscosity. Journal of Scientific Computing, 49(1):35–50, 2011.

[1]Laboratoire d'Informatique pour la Mécanique et les Sciences de l'Ingénieur, LIMSI, CNRS, Univ. Paris-Sud, Université Paris-Saclay, Bât 508, Campus Universitaire F-91405 Orsay; [2]Department of Mathematics, Texas A&M University 3368 TAMU, College Station, TX 77843-3368, USA; [3]Luth, Observatoire de Paris-Meudon, place Janssen, 92195-Meudon, France.

E-mail address: caroline.nore@limsi.fr